ARTICLE

Coherent quantum dynamics of systems with coupling-induced creation pathways

Steven D. Rogers[1,2], Austin Graf[2,3,5], Usman A. Javid[2,3,5] & Qiang Lin[2,3,4]

Many technologies emerging from quantum information science heavily rely upon the generation and manipulation of entangled quantum states. Here, we propose and demonstrate a new class of quantum interference phenomena that arise when states are created in and coherently converted between the propagating modes of an optical microcavity. The modal coupling introduces several new creation pathways to a nonlinear optical process within the device, which quantum mechanically interfere to drive the system between states in the time domain. The coherent conversion entangles the generated biphotons between propagation pathways, leading to cyclically evolving path-entanglement and the manifestation of coherent oscillations in second-order temporal correlations. Furthermore, the rich device physics is harnessed to tune properties of the quantum states. In particular, we show that the strength of interference between pathways can be coherently controlled, allowing for manipulation of the degree of entanglement, which can even be entirely quenched. The states can likewise be made to flip-flop between exhibiting initially correlated or uncorrelated behavior. The phenomena presented here open a route to creating higher dimensional entanglement and exotic multi-photon states.

[1] Department of Physics and Astronomy, University of Rochester, Rochester, NY 14627, USA. [2] Center for Coherence and Quantum Optics, University of Rochester, Rochester, NY 14627, USA. [3] Institute of Optics, University of Rochester, Rochester, NY 14627, USA. [4] Department of Electrical and Computer Engineering, University of Rochester, Rochester, NY 14627, USA. [5]These authors contributed equally: Austin Graf, Usman A. Javid. Correspondence and requests for materials should be addressed to Q.L. (email: qiang.lin@rochester.edu)

Aworldwide effort is underway to unlock the practical and potentially transformative utilities of quantum systems[1–7]. If successful, a broad range of fields stand to be revolutionized, including information processing[1,8–11], simulation[12], communication[13], security[14,15], and metrology[16,17]. Moreover as with many nascent technological revolutions, it is not immediately clear, which architectures will prove most useful in realizing these developments. It is, however, without doubt that the efficacy of such systems is linked to how proficiently they can generate and manipulate quantum states and their entanglement. To this end, it is especially important that new concepts are developed, which carry out these functions while remaining broadly implementable.

As a result of the research interest in this area, numerous methods have been established to generate and manipulate quantum states. A particularly promising approach involves the quantum interference of multiple excitation/creation pathways, which coherently drives a system between states in the time domain. These processes have led to a diverse set of important phenomena, including governing the dynamics of electron spins in semiconductors[18], many-body oscillations in cold atoms[19], superconducting flux qubits in Josephson junctions[20], inversionless laser oscillations in atomic media[21], and polarization entanglement between photon pairs emitted from biexcitons[22], to name a few. Here, we propose and demonstrate a new class of quantum interference phenomena that result when quantum states are created in and coherently converted between propagating electromagnetic cavity modes. We realize this concept by implementing a nonlinear optical process between the coupled counter-propagating modes of a microresonator—establishing multiple energy-level pathways for photon pair creation. In doing so, we are able to generate tunable photonic quantum states, which are imparted with intrinsic time-evolving path-entanglement and exhibit coherent oscillations in their second-order temporal correlations. In particular, we show that the ability to conveniently tune properties of the optical microresonator translates to a powerful platform for manipulating the state and its entanglement properties via quantum interference. Furthermore, we demonstrate that varying the cavity photon lifetime transforms the system from producing strongly entangled quantum states of light with extremely high-contrast two-photon interference visibility, to a regime where the entanglement and oscillations are quenched and the photon statistics return to the behavior of an uncoupled system. The device may also be configured to flexibly set the probability amplitudes associated with generating photon pairs in one or the other propagation modes, thus providing a means to explore how internal symmetry affects the quantum state and entanglement.

Results

Coupling-induced creation pathways. We implement the concept within a whispering-gallery mode (WGM) microresonator that supports spontaneous four-wave mixing (SFWM), a $\chi^{(3)}$ nonlinear optical process[23], between three interacting cavity modes (see Fig. 1). As shown in Fig. 1a, b, photons are coupled from a forward-propagating pump into the pump (p) mode alone, but may spontaneously scatter into the adjacent signal (s) and idler (i) modes, in accordance with energy conservation. When weakly pumped, this vacuum-seeded nonlinear wave mixing process produces correlated bipartite states[24,25].

Rotationally symmetric microresonators support two degenerate modes for each resonance frequency, forward (clockwise) and backward (counterclockwise) traveling, which do not exchange energy in the absence of coupling[26]. Thus, when
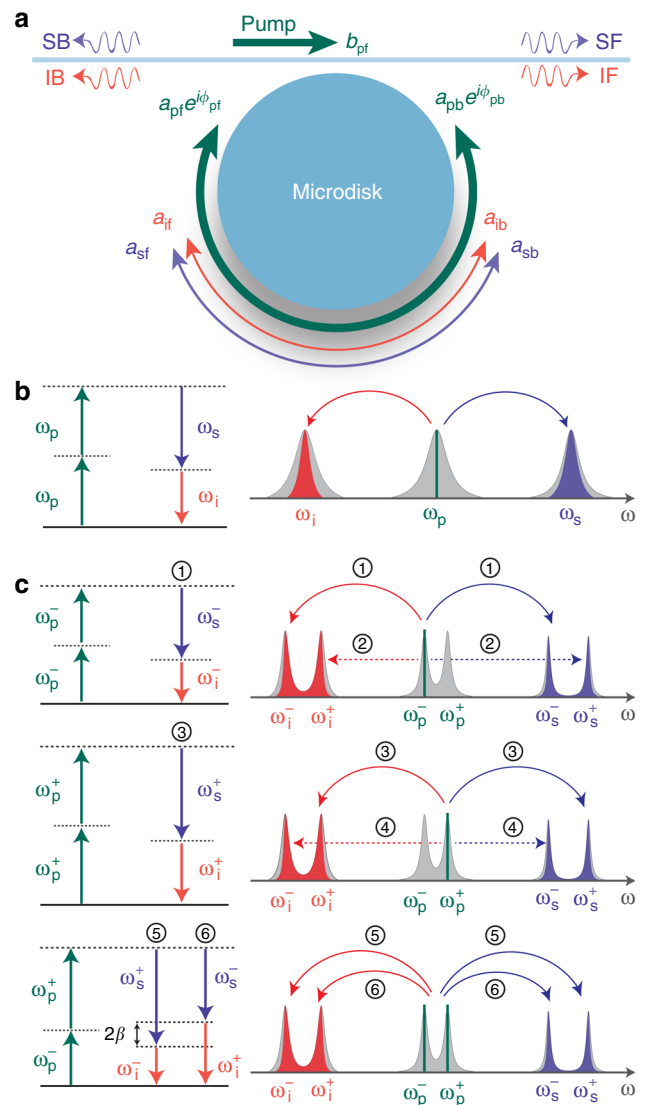
Fig. 1 Photon pair creation between coherently coupled counter-propagating whispering-gallery modes (WGMs). **a** A forward-propagating pump wave (green) evanescently couples into the microdisk, on resonance with the pump cavity mode, building up a strong intracavity field in the forward direction, a_{pf}. In the presence of degenerate mode coupling, the backward-traveling intracavity pump field, a_{pb}, also experiences a coherent buildup. Through spontaneous four-wave mixing (SFWM), signal (blue) and idler (red) photons are created between their respective coherently coupled forward and backward intracavity modes, establishing tunable photonic quantum states with time-evolving path-entanglement. The photon pairs are coupled from the cavity into four transmitted fields: signal forward (SF), signal backward (SB), idler forward (IF), and idler backward (IB). Hence, correlations are established between photon pairs in the four path configurations: SF-IF, SF-IB, SB-IF, SB-IB. **b** Energy diagram and spectral emission profiles for SFWM in an uncoupled optical microresonator. **c** Energy diagrams and spectral emission profiles for SFWM between coupled counter-propagating WGMs. Green lines indicate which pairs of pump photons are annihilated for the various creation pathways. The dashed creation pathways are only relevant for extremely short timescales, as permitted by the uncertainty principle

photons are generated inside an uncoupled microcavity they are restricted to remain in a single propagation mode and are the result of a single creation pathway (see Fig. 1b), precluding quantum interference. If, however, a coupling is introduced
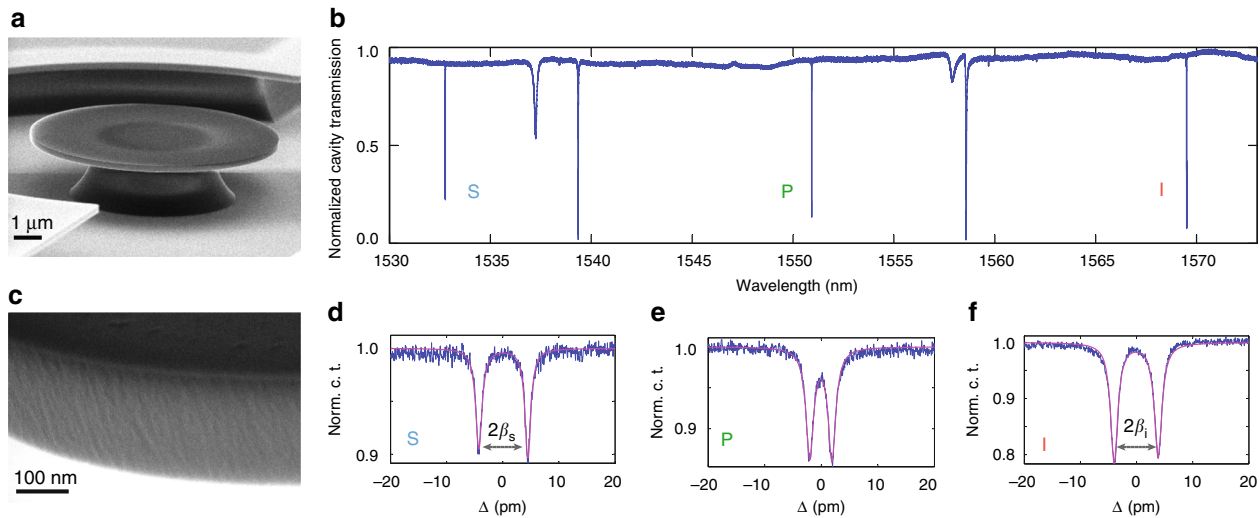
Fig. 2 Characterization of the silicon microdisk and coupling-induced resonance splitting. **a** A scanning electron microscope (SEM) image of the silicon microdisk suspended via a silica pedestal. **b** Normalized cavity transmission spectrum with labels, indicating the signal (S), pump (P), and idler (I) modes used in the cavity-enhanced spontaneous four-wave mixing (SFWM) process. **c** High-magnification SEM image of the device in **a**. Here, we observe the nanometer-scale surface roughness, which mediates the Rayleigh-scattering-induced coupling between counter-propagating modes. **d**–**f** Detailed versions of the signal, pump, and idler doublet transmission profiles (blue), respectively, along with the fits (magenta) used to extract intrinsic optical Qs and modal coupling rates. Δ: Detuning

between the counter-propagating modes, then the proposed phenomena may be realized through the establishment of a coherent conversion process. In the specific implementation considered here, photons are converted between the forward (f) and backward (b) propagation modes at a rate of β_m (m = p, s, i), which is revealed through, $H_0 = \sum_m \{\hbar\omega_{0m}(a_{mf}^\dagger a_{mf} + a_{mb}^\dagger a_{mb}) - \hbar(\beta_m a_{mf}^\dagger a_{mb} + \beta_m^* a_{mb}^\dagger a_{mf})\}$, the unperturbed Hamiltonian (see Supplementary Note 1 for the complete Hamiltonian).

One of the key consequences of modal coupling is that it erases the 'which-path' information from the system. For instance, when a photon exits the device it is fundamentally impossible to know whether it was originally generated in that propagation direction or converted from the counter-propagating mode. The same rule applies to its correlated partner photon, which together form the bipartite state. Thus, the probability amplitudes describing these alternative pathways add coherently, enabling quantum interference[27]. To gain further insight into how modal conversion affects the system, we start by examining H_0. The coupling-induced energy splitting is apparent after diagonalization, which here, amounts to rotating to a standing-wave basis with eigenvectors composed of symmetric and antisymmetric combinations of traveling waves, and shifted eigenfrequencies, $\omega_{0m}^\pm = \omega_{0m} \pm |\beta_m|$. By applying the same transformation to the interaction Hamiltonian, we uncover how the coupling modifies the nonlinear optical processes responsible for generating the tunable photonic quantum states. In the standing-wave basis, the interaction Hamiltonian becomes $H_{int} = \frac{\hbar}{2}g(a_{s-}^\dagger a_{i-}^\dagger + a_{s+}^\dagger a_{i+}^\dagger)(a_{p-}^2 + a_{p+}^2) + \hbar g(a_{s-}^\dagger a_{i+}^\dagger + a_{s+}^\dagger a_{i-}^\dagger)a_{p-}a_{p+} + h.c.$, where g is the vacuum coupling rate for the SFWM process. Here, we see the diverse set of photon creation pathways that result from the coherent conversion between modes (see Fig. 1c and Supplementary Note 2).

Another critical feature of modal coupling is the effect it has on the driving field. Although a single external pump is provided, the device splits it into two counter-propagating cavity modes (see Fig. 1a). Now, pairs of photons from either the forward or backward pump modes can participate in the nonlinear optical process. Furthermore, the modal conversion is coherent, and

therefore establishes a definite phase between them. To satisfy conservation of angular momentum[23], photon pairs are only created in the co-propagating states. Thus, if we assume an undepleted classical pump and closed system, the photonic quantum states generated within the cavity will be of the form, $|\psi(t=0)\rangle = c_f|f\rangle_s|f\rangle_i + c_b|b\rangle_s|b\rangle_i$, where $t=0$ denotes the time of creation, and the complex coefficients, c_f and c_b are set by properties of the pump modes (see Supplementary Note 2). However, forward and backward are not eigenstates of the coupled cavity, and thus evolve in time, resulting in a versatile quantum state (see Supplementary Note 3),

$$\begin{aligned}|\psi(t)\rangle = & (c_f\cos^2(\beta t) - c_b\sin^2(\beta t))|f\rangle_s|f\rangle_i \\ & + (c_b\cos^2(\beta t) - c_f\sin^2(\beta t))|b\rangle_s|b\rangle_i \\ & + i(c_f + c_b)\sin(2\beta t)(|f\rangle_s|b\rangle_i + |b\rangle_s|f\rangle_i),\end{aligned} \quad (1)$$

where we have assumed equal coupling rates for the pump, signal, and idler modes. In the case that $c_f = c_b$, then we clearly see the evolution through different Bell states inside the cavity. For instance, at $t=0$, the state is composed of maximally entangled co-propagating photons, $|\psi(t=0)\rangle \propto |f\rangle_s|f\rangle_i + |b\rangle_s|b\rangle_i$, whereas at $t = \pi/(4\beta)$, the state is composed of maximally entangled counter-propagating photons, $|\psi(t=\pi/(4\beta))\rangle \propto |f\rangle_s|b\rangle_i + |b\rangle_s|f\rangle_i$.

Device realization. There are numerous systems that may be used to achieve photon generation between coupled counter-propagating modes. Here, we have chosen to demonstrate this phenomenon in a high-Q silicon microdisk. In recent years, there has been interest in silicon microresonators as chip-scale sources, because they can produce ultra-pure photon pairs with high-spectral brightness, strong temporal correlations, and emission wavelengths in the telecommunications band[28–35]. Additionally, they may be fabricated using complementary metal-oxide-semiconductor (CMOS) compatible processes, indicating the possibility of mass manufacturing[36].

A scanning electron microscope (SEM) image of our suspended silicon microdisk, with a radius of approximately 4.5 μm and thickness of 260 nm, is shown in Fig. 2a. In Fig. 2b we plot the normalized cavity transmission, which exhibits multiple

quasi-transverse-magnetic (quasi-TM) mode families, with the pump (p) at $\lambda_p = 1550.6$ nm, signal (s) at $\lambda_s = 1532.5$ nm, and idler (i) at $\lambda_i = 1569.2$ nm. Frequency matching among the interacting cavity modes is achieved by engineering the group-velocity dispersion of the device, consequently enabling efficient SFWM. The nanometer-scale roughness at the surface of the microdisk (see Fig. 2c) mediates Rayleigh scattering between the traveling modes, leading to a coherent coupling[37], as is evidenced by the formation of doublets in the transmission profiles (see Fig. 2d–f). The intrinsic optical Qs for the pump, signal, and idler resonances are extracted from fits of the doublets in Fig. 2d–f, and are, respectively, found to be, $Q_{0p} = 1.27 \times 10^6$, $Q_{0s} = 1.32 \times 10^6$, and $Q_{0i} = 1.15 \times 10^6$. Additionally, the doublet splittings for the signal and idler modes are, respectively, found to be $2\beta_s/2\pi = 1.11$ GHz and $2\beta_i/2\pi = 0.97$ GHz. The modes exhibit extremely low-intrinsic photon decay rates ($\Gamma_0 = \omega_0/Q_0$) of $\Gamma_{0p}/2\pi = 0.15$ GHz, $\Gamma_{0s}/2\pi = 0.14$ GHz, and $\Gamma_{0i}/2\pi = 0.16$ GHz, due to the high quality of the single-crystalline silicon and optimization of the fabrication process. We now see the dual role that the high-Q cavity assumes in our system. Here, the cavity-enhancement serves to greatly strengthen the efficiency and purity of the photon generation process and effectively modifies the Rayleigh scattering cross section[38,37], such that scattering is highly preferential between counter-propagating modes. Hence, photon pairs are created within the cavity and experience a strong coherent coupling between the forward and backward modes, providing a convenient platform for demonstrating the proposed quantum interference phenomena.

Quantum interference and coherent oscillations. Under the assumption of a closed system, the quantum states created within our device exhibit cyclically evolving path-entanglement (see Eq. (1)). We now consider what happens when the states are subjected to intrinsic loss, Γ_{0m} ($m = s, i$), and are allowed to leave the microdisk at an external coupling rate, Γ_{em}. Photon pairs are consequently transmitted into the two propagation directions of the optical waveguide (see Fig. 1a) and establish the following single photon pathways: signal forward (SF), signal backward (SB), idler forward (IF), and idler backward (IB). Moreover, the cyclically evolving path-entanglement within the device manifests as temporal correlations, which coherently oscillate between pairs of propagation pathways, as seen in (see Supplementary Note 4),

$$p(t_{sj}, t_{ik}) = N e^{-\Gamma_{tm}|\tau|} |\zeta_m^{jk} \cos(\beta_m \tau) + \eta_m^{jk} \sin(\beta_m \tau)|^2 \quad (2)$$

where t_{sj} (j = f, b) and t_{ik} (k = f, b) respectively denote the times at which the signal and idler photons are emitted from the microdisk. The subscript m = s when $t_{sj} > t_{ik}$, and m = i when $t_{sj} < t_{ik}$. N is a constant quantifying properties of the device (see Supplementary Note 4), $\Gamma_{tm} = \Gamma_{0m} + \Gamma_{em}$ is the total photon decay rate, and $\tau \equiv t_{sj} - t_{ik}$ denotes the delay between signal and idler emission times. The strength of the oscillatory terms in Eq. (2) are, respectively, governed by $\zeta_m^{jk} = c_{m1}^{jk} |a_{pf}|^2 e^{-i\phi} - c_{m2}^{jk} |a_{pb}|^2$ and $\eta_m^{jk} = c_{m3}^{jk} |a_{pf}|^2 e^{-i\phi} - c_{m4}^{jk} |a_{pb}|^2$, with $|a_{pf}|^2$ and $|a_{pb}|^2$ being the energy contained in the forward and backward pump cavity modes, and ϕ defining their relative phase. The c_{mn}^{jk} (n = 1 to 4) are constants defined by the coupling and decay rates of the modes (see Supplementary Note 4). The compact notation used in Eq. (2) emphasizes that although there are many intricate interactions occurring within the device, the pair correlations broadly consist of three main components, in that, they oscillate within a decay envelope set by the cavity photon lifetime, exhibit an oscillation frequency, which matches the modal coupling rate, and are manipulated by interfering the counter-propagating intracavity pump waves.
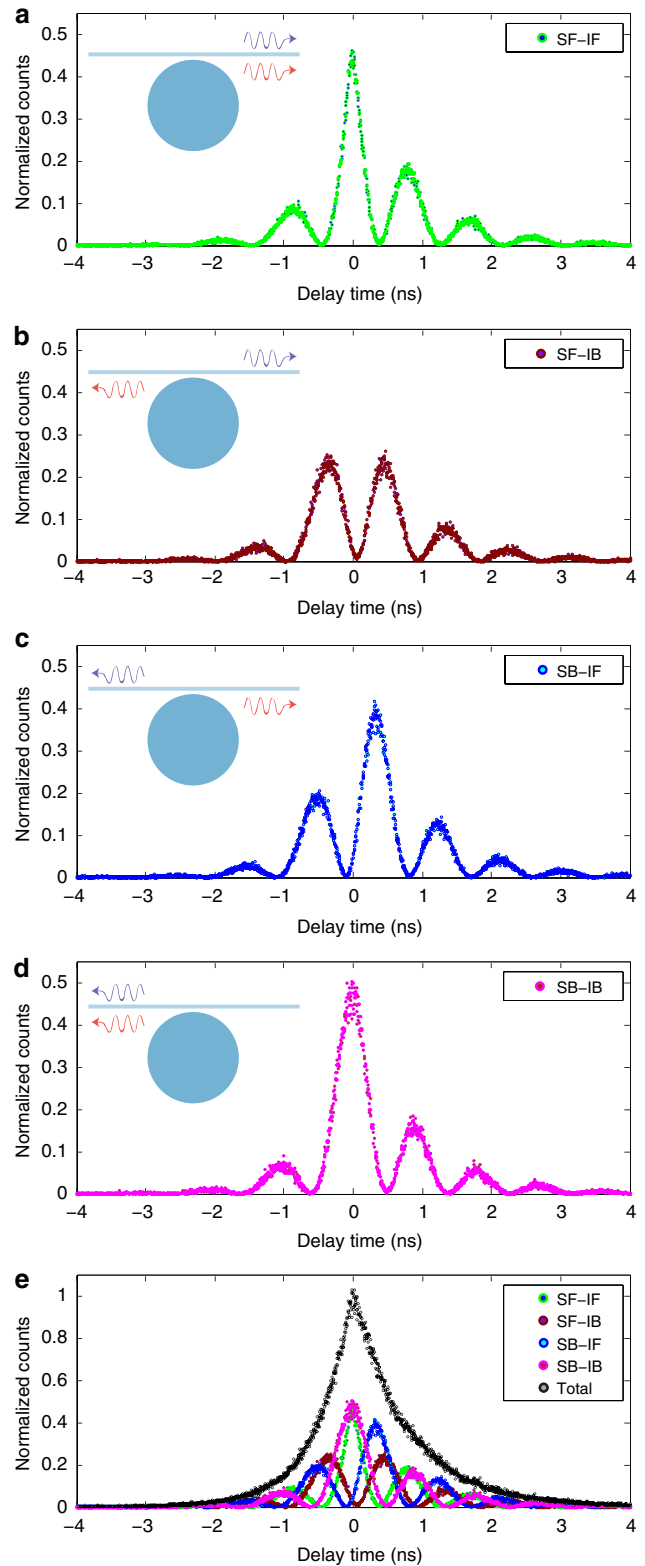
Fig. 3 Coherent oscillations in pair correlations via quantum interference of multiple creation pathways. Cross-correlation waveforms (without background subtraction), measured between **a** signal forward-idler forward (SF-IF), **b** signal forward-idler backward (SF-IB), **c** signal backward-idler forward (SB-IF), and **d** signal backward-idler backward (SB-IB). **e** All pair correlations superposed on a single delay-time axis with the decay envelope in black resulting from the numeric sum of coincidence counts at each time bin. All data are normalized to the peak of the decay envelope. Insets depict path configuration
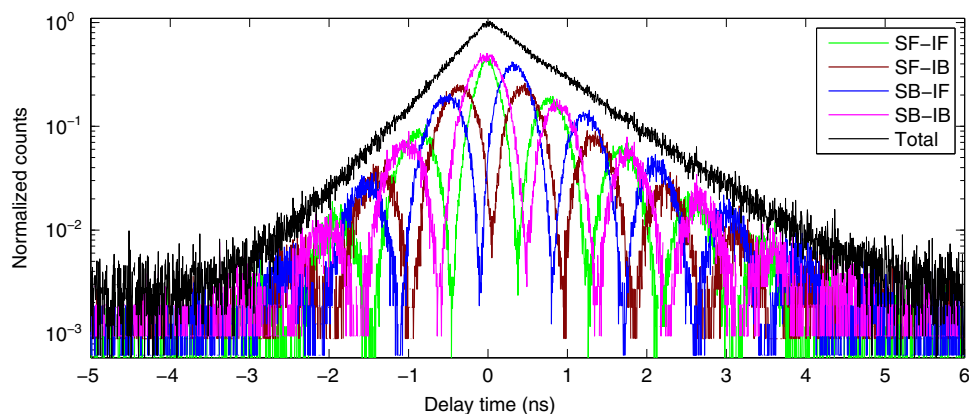
Fig. 4 Time-evolving path-entanglement and high-contrast two-photon interference visibility. Here, we show the logarithmic scaling of pair correlations from all four path configurations superposed onto a single delay-time axis. The photon decay envelope, shown in black, results from the numeric sum of coincidence counts at each time bin. The strong quantum entanglement is observed through the coherent transfer of biphoton correlations between co-propagating (SF-IF (green) & SB-IB (magenta)) and counter-propagating (SF-IB (brown) & SB-IF (blue)) states of the system

The total photon decay rate is conveniently tuned by varying the gap between the microdisk and waveguide. Initially, we set the total photon decay rate to be significantly less than the modal coupling rate and record the pair correlations for each of the four path configurations (signal forward-idler forward (SF-IF) in Fig. 3a, signal forward-idler backward (SF-IB) in Fig. 3b, signal backward-idler forward (SB-IF) in Fig. 3c, and signal backward-idler backward (SB-IB) in Fig. 3d). The measured correlations exhibit striking differences when compared to the monotonically decaying correlations between photon pairs from all other chip-scale sources studied to date. As predicted (see Eq. (2)), the photon pairs in each of the path configurations exhibit coherent oscillations with estimated oscillation frequencies that are in good agreement with the measured doublet splittings. Furthermore, we see that biphotons in the co-propagating states (SF-IF and SB-IB) are highly correlated at zero delay-time and then oscillate between being highly correlated and uncorrelated (Fig. 3a, d). In contrast, a complementary effect is observed between biphotons in the counter-propagating states (SF-IB & SB-IF) (Fig. 3b, c). Taken together, it is apparent that as pair correlations are diminishing in one state they are intensifying in another, and vice versa. To precisely characterize this relationship, we superpose the correlations from each path configuration and numerically sum the coincidence counts at each time bin, resulting in the black correlation waveform (Fig. 3e). Here, we observe that the pair correlations from all four states perfectly sum to give an exponential decay envelope, as predicted in Eq. (2).

The logarithmic scaling in Fig. 4 confirms the exponential nature of the photon decay envelope and reveals that the quantum interference responsible for driving the time-domain oscillations is of extremely high visibility. Here, we clearly observe that each of the correlation waveforms exhibit extinction ratios approaching or >20 dB. Additionally, we see that the coincidence counts from the co-propagating states are almost completely out of phase with the counts from the counter-propagating states, suggesting that path-entanglement is present in the system. Recently, Du and colleagues[39] showed that the arrival times between pairs of detection events may be used as a local parameter setting for entanglement measurements in systems where the photon coherence times are much longer than the timing resolution of the detectors. Owing to the high-Q nature of our microcavity, the photon coherence times here are on the order of nanoseconds, whereas the timing resolution of the superconducting detectors (see Methods) are only tens of picoseconds. Consequently, by varying delay-time as an analog

of phase, we record a Bell parameter (see Supplementary Note 5) of $S = 2.80 \pm 0.07$, which yields a Bell violation[40,41] of eleven standard deviations, confirming the path-entanglement predicted in Eq. (1).

Modal coupling vs. photon decay rate. A common feature among coherently coupled systems is the expression of markedly different behavior between the weak and strong coupling regimes[42–44]. We explore these boundaries in Fig. 5, with the experimental data presented on the left half of the figure (Fig. 5a–c) and the corresponding theory plots on the right (Fig. 5d–f and see Supplementary Note 6 for more details).

By tuning the total photon decay rate, we significantly manipulate the intracavity quantum state, as is evidenced by the response of the pair correlations in Fig. 5. With the decay rate set to be less than the modal coupling rate, we experimentally observe the strong coupling regime, as shown in Fig. 5a. Here, we see several high-contrast oscillations resulting from the strong quantum interference and path-entanglement. When the coupling and decay rates are similar, as is shown in Fig. 5b, there are fewer oscillations, due to the diminished biphoton lifetime. Additionally, the pairs of correlation waveforms belonging to the same state classification—co-propagating vs. counter-propagating —share less similarity than in Fig. 5a. To explain this phenomenon, we note that changing the decay rate also changes the relationship between intracavity pump modes. In Fig. 5a, the intracavity energies contained in the forward and backward pump modes are closer to being equalized, leading to a more symmetric system with respect to state generation, and consequently greater similarity between the pairs of waveforms within the same state classification. In the special case that the energies contained in the intracavity pump modes were exactly equal, then the pairs of correlation waveforms from the same state classification would be indistinguishable (see Supplementary Note 7). When the decay rate is set to be much greater than the coupling rate, we enter the weak coupling regime where the correlation waveforms exhibit pure monotonic decay, as shown in Fig. 5c. In this extreme scenario, the quantum inference, path-entanglement and coherent oscillations are quenched as a result of tuning the biphoton state until it assumes the form of those produced in uncoupled systems.

The experimental results agree well with the theoretical predictions in Fig. 5. The small discrepancies are likely due to the presence of slight asymmetries in the doublet transmission profiles of the interacting cavity modes (see Fig. 2d–f).
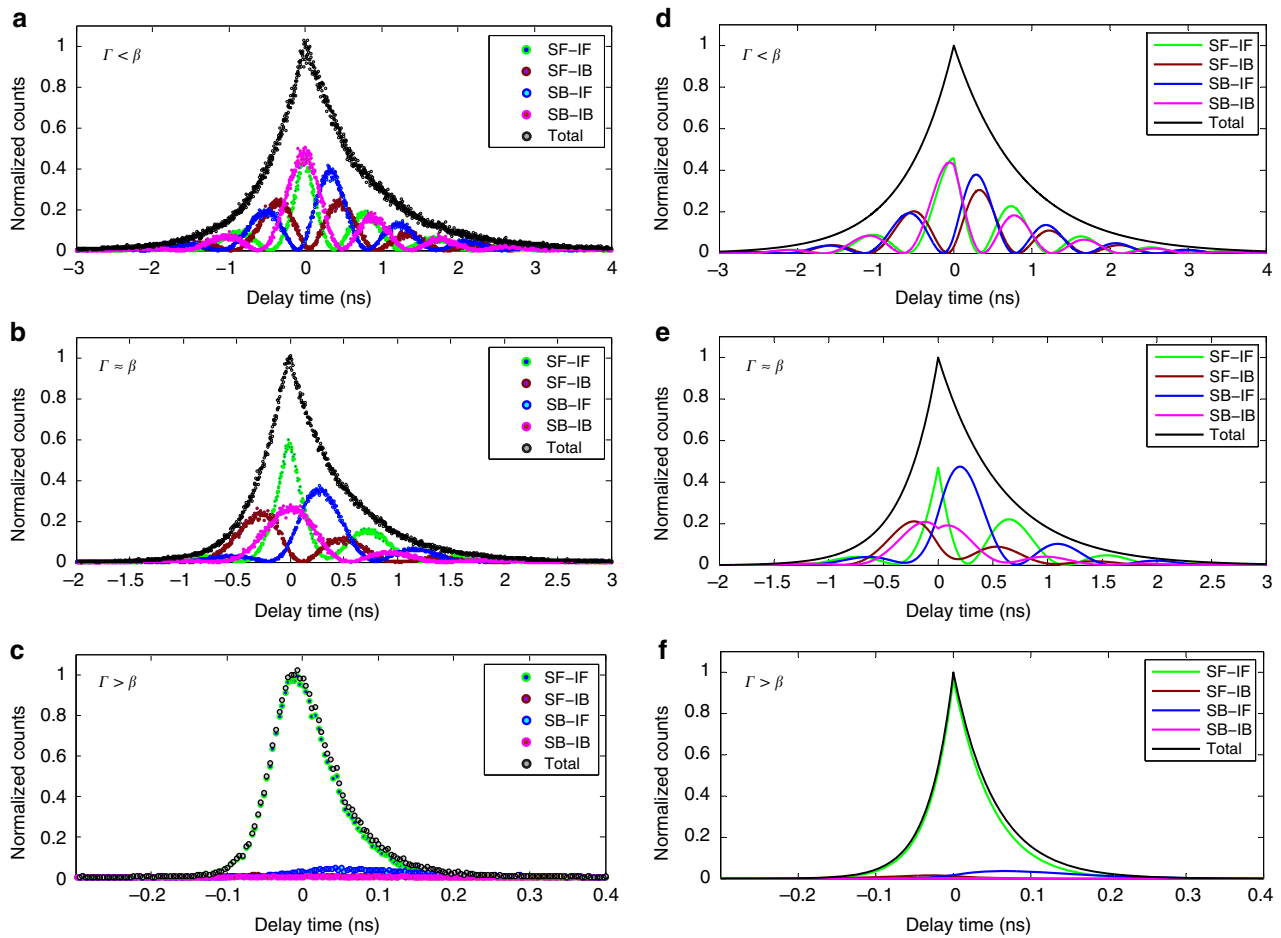
Fig. 5 Manipulating the quantum state and entanglement by tuning the cavity photon lifetime. Measured pair correlations (without background subtraction) for each path configuration with the total photon decay set to be **a** less than the modal coupling rate, **b** similar to the modal coupling rate, and **c** greater than the modal coupling rate. **d–f** Theory plots corresponding to the experimental data in **a–c**, respectively. In each figure, cross-correlation waveforms between signal forward-idler forward (SF-IF) are shown in green, signal forward-idler backward (SF-IB) are shown in brown, signal backward-idler forward (SB-IF) are shown in blue, and signal backward-idler backward (SB-IB) are shown in magenta. The decay envelopes, shown in black, result from the numeric sum of coincidence counts from all path configurations at each time bin. All data are normalized to the peak of the photon decay envelope. The photon pairs are detected at a coincidence rate of $(3.107 \pm 0.004) \times 10^2$ Hz in **a**, $(2.911 \pm 0.004) \times 10^3$ Hz in **b**, and $(2.44 \pm 0.01) \times 10^2$ Hz in **c**. The photon pairs exhibit a Bell parameter of $S = 2.80 \pm 0.07$ in **a**, $S = 2.60 \pm 0.11$ in **b**, and $S = 1.50 \pm 0.13$ in **c**. We note that the biphoton coherence time in **c** is comparable to the detector response time, which causes the measured waveforms to display a Gaussian shape

Furthermore, it is possible that a small amount of free-carrier absorption occurs at the pump powers used in the experiment. These effects are discussed in greater detail in Supplementary Note 6.

Pump-induced quantum interference. The interacting cavity modes each experience the same type of modal coupling. However, we emphasize that the coupling of pump modes uniquely affects the system, as they are the progenitors of the creation process. Moreover as such, tuning properties of the coupled pump modes translates to directly manipulating the intracavity quantum state (see Eq. (1)) and the correlations that consequently manifest (see Eq. (2)).

Changing the frequency of the external pump laser (ω_L) relative to the resonance frequency of the pump cavity mode (ω_{0p}) introduces a detuning, $\Delta = \omega_L - \omega_{0p}$, to the system. When the detuning is swept, the coupled pump modes display the well-established doublet transmission profile, as seen in Fig. 6a. Importantly, varying the detuning induces a phase change between the intracavity pump modes in a manner analogous to a driven harmonic oscillator. Owing to the high-Q nature of the

cavity, a small amount of detuning about resonance enables a π relative phase shift, as shown in Fig. 6b. Thus, the coupled system naturally admits two regimes of operation, negative detuning (see points (1)–(4) in Fig. 6a, b) and positive detuning (see points (5)–(8) in Fig. 6a, b), with a significant phase change between them. We note that these changes are an internal response of the coupled system, and thus, are achieved without requiring a second external laser coupled to the counter-propagating mode.

The effects described above and illustrated in Fig. 6a, b are purely classical with regards to the pump mode alone. However, considering the system as a whole reveals the manner in which the pump-coupling induces quantum interference. Without coupling, there is no backward-propagating pump, and setting the corresponding coefficients to zero in the quantum state (see Eq. (1)) and pair correlations (see Eq. (2)) removes the mechanism to directly change their form. In this case, the system still exhibits quantum interference, but it does so in a fixed configuration. When the pump modes are coupled, it enables coherent control over the strength of interference between creation pathways, adding a dynamic feature to the system. Thus, sweeping the detuning causes pump-induced
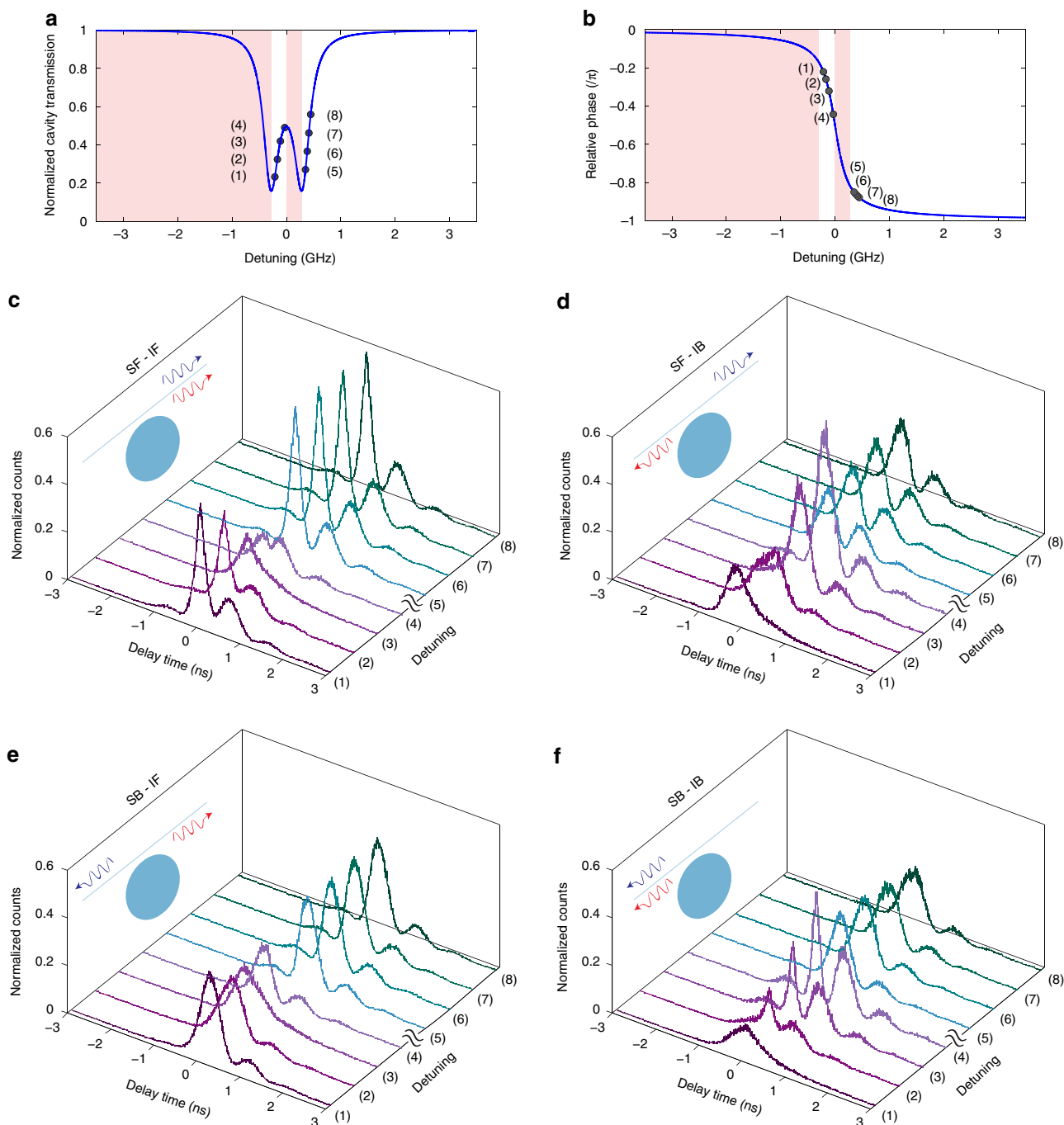
Fig. 6 Tuning the intracavity quantum state through pump-induced quantum interference. Theoretical plots of the pump **a** transmission profile and **b** relative phase between counter-propagating modes. The external laser is locked to the pump cavity mode at points (1)–(8), which correspond to detuning values of $\Delta/2\pi = (-0.21, -0.16, -0.11, -0.06, 0.35, 0.38, 0.41, 0.44)$ GHz, respectively, and denote the values appearing in **c**–**f**. The laser locking is achieved through the thermo-optic feedback method where the light-red shading indicates the unstable locking regions. Cross-correlation waveforms (without background subtraction), measured between **c** signal forward-idler forward (SF-IF), **d** signal forward-idler backward (SF-IB), **e** signal backward-idler forward (SB-IF), and **f** signal backward-idler backward (SB-IB) are plotted as a function of detuning between the pump laser and resonance frequency of the pump cavity mode. Note that the waveforms within each stacked plot are offset by an equal spacing to aid in viewing clarity. Insets depict path configuration

quantum interference, which significantly manipulates the intracavity quantum state. This effect clearly manifests in the variable response of the pair correlations shown in Fig. 6c–f. In fact, the interference is so strong that changing from negative to positive detuning (point (4) to (5)) causes the SF-IB (see Fig. 6d) and SB-IF (see Fig. 6e) states to flip from exhibiting highly correlated to completely uncorrelated behavior near zero

delay-time. Detailed versions of this transition, for each path configuration, may be seen in Supplementary Note 8.

Discussion

In this work, we proposed and demonstrated a new set of quantum interference phenomena that result from the creation

and coherent conversion of quantum states between the propagating modes of an optical microcavity. The resulting photonic quantum states are highly versatile and exhibit cyclically evolving path-entanglement. Importantly, we showed that the states and entanglement are greatly manipulated by controlling parameters of the device. We envision that the concepts presented here will have broad impacts relating to quantum state generation and novel entanglement properties, particularly in the field of quantum information processing. To demonstrate the underlying physics of the quantum interference phenomena, the waveguide-microdisk coupling was tuned over a large range (see Fig. 5). In practical applications, it is generally desirable to over-couple the device so that the photons are efficiently extracted from the cavity. This coupling condition can be achieved while maintaining a high degree of path-entanglement in devices with sufficient intrinsic optical Q and/or resonance splitting.

We note that the coupling of counter-propagating modes was achieved through Rayleigh scattering, which relies upon the existence of roughness at the surface of the device. Alternatively, the coupling could be established by bringing a nanoscale probe in contact with the device[45], or through a technique called selective mode splitting (SMS), which couples counter-propagating modes by matching their azimuthal mode number with a periodic modulation along the perimeter of the microresonator[46]. These techniques would extend the concepts presented here to devices made from ultra-smooth materials and have the additional benefit of providing a means to control and tune the coupling rates.

We showed that a single external laser can directly manipulate the quantum state through pump-induced quantum interference. Alternatively, the laser could be split and coupled into the device from both directions, which would precisely control the amplitude and phase relationship between the internal pump modes independent of the cavity properties. This added feature would enable complete control over the quantum state (see Eq. (1)) and perfect pump-induced quantum interference visibility (see Supplementary Note 7). Additionally, this type of state manipulation would manifest in the coherent oscillations as a phenomenon akin to the Rabi flop operations that are used to optically prepare and control electron spins in solid-state systems[47].

Looking forward, a particularly intriguing follow-up involves building upon the capabilities of a single device by combining many devices in a large-scale photonic quantum circuit. Device to device and device to waveguide interactions could then be established and flexibly controlled through the addition of micro-electro-mechanical (MEMS) actuators, phase shifters, and microheaters, among other commonly used integrated photonics components. Based upon the observations made in this work, it is envisioned that such an architecture could be used to create exotic multi-photon states with fascinating properties, including controllable multi-partite entanglement and topologically protected quantum state transfer[48].

Methods

Device fabrication. The microdisk device is fabricated from a silicon-on-insulator wafer with a top silicon layer of 260 nm and buried oxide thickness of 2 μm. The initial device pattern is written into a high-resolution electron-sensitive resist (ZEP 520A) using electron-beam lithography. The pattern is then transferred to the silicon layer through an inductively coupled-plasma (ICP) reactive-ion-etch (RIE), utilizing a SF_6/C_4F_8 gas chemistry. Finally, the buried oxide layer is removed by wet etching in hydrofluoric (HF) acid, yielding the suspended microdisk device seen in Fig. 2a.

Pair generation and photon statistics. A continuous-wave tunable pump laser (Santec TSL-550C) is transmitted through a course-wavelength-division-multiplexing (CWDM) multiplexer (MUX), having a 3-dB bandwidth of 17 nm

and band isolation exceeding 120 dB, in order to prevent amplified spontaneous emission (ASE) from leaking into the single photon channels. The filtered pump light is then evanescently coupled from a tapered optical fiber into the device, using a nano-positioning set-up. The polarization state at the point of coupling is controlled using fiber polarization controllers (FPC) in order to excite the cavity modes. The cavity modes utilized in the experiment are second-radial-order quasi-transverse-magnetic (quasi-TM2) and exhibit a free spectral range of 2.29 THz. Photon pairs are coupled from the microdisk back into the tapered optical fiber (see Fig. 1a) in both the forward and backward directions and separated using CWDM demultiplexers. The demultiplexed pump beam is detected using a fast photodector, which allows for continuous monitoring of the coupled optical power, laser-cavity detuning, and implementation of the thermo-optic locking method[49]. The signal and idler photons, from both propagation directions, are then passed through standard telecom optical switches in order to select the four path configurations based on the switch settings. The photons exiting the switches are passed through tunable bandpass filters (TBPF), having a 3-dB bandwidth of 1.2 nm, in order to suppress the Raman noise photons that are generated throughout the input side of the optical fiber. The single photons are then detected using two superconducting nanowire single photon detectors (SNSPD, Single Quantum), which have extremely small timing jitters of 16 ps and detection efficiencies of 54%.

The input optical power is set to $P_{in} = 8.54$ μW for all experimental data presented here, and the optical power coupled into the pump cavity mode ranges from $P_{d,min} = 4.46$ μW to $P_{d,max} = 6.44$ μW, as a function of laser-cavity detuning. Photon pairs are produced at a total pair generation rate of $(4.078 \pm 0.005) \times 10^4$ pairs s^{-1} for the data appearing in Figs. 3, 4, and 5a, $(3.751 \pm 0.005) \times 10^5$ pairs s^{-1} for the data appearing in Fig. 5b, and $(4.54 \pm 0.02) \times 10^4$ pairs s^{-1} for the data appearing in Fig. 5c. In Fig. 6, the total pair generation rate varies from a minimum of $(1.928 \pm 0.003) \times 10^5$ pairs s^{-1} to a maximum of $(4.654 \pm 0.005) \times 10^5$ pairs s^{-1} as a function of laser-cavity detuning. The photon arrival times are recorded using the time-tagged mode of a time-correlated single-photon counter (TCSPC, PicoHarp 300) with time bins of 4 ps. The correlation waveforms appearing in Figs. 3, 4, and 5a were acquired over a period of $T_{acq} = 1800$ s. The correlation waveforms appearing in Figs. 5b, c and 6 were acquired over a period of $T_{acq} = 200$ s. The transmittance (including the tapered-fiber loss and insertion loss of all components from the device to the detectors) associated with each single-photon pathway is given as follows: $\eta_{sf} = 0.21$ for signal forward, $\eta_{sb} = 0.21$ for signal backward, $\eta_{if} = 0.20$ for idler forward, and $\eta_{ib} = 0.15$ for idler backward. All coincidence counts presented in the Article are normalized to the peak of their respective decay envelope. A schematic of the experimental set-up may be found in Supplementary Note 9.

Data availability
The data that support the plots and other findings within this paper are available from the corresponding author upon reasonable request.

References
1. O'Brien, J. L., Furusawa, A. & Vuckovic, J. Photonic quantum technologies. *Nat. Photonics* **3**, 687–695 (2009).
2. Kurizki, G. et al. Quantum technologies with hybrid systems. *Proc. Natl Acad. Sci. USA* **112**, 3866–3873 (2015).
3. Heshami, K. et al. Quantum memories: emerging applications and recent advances. *J. Mod. Opt.* **63**, 2005–2028 (2016).
4. Acin, A. et al. The quantum technologies roadmap: a European community view. *New J. Phys.* **20**, 080201 (2018).
5. Awschalom, D. D., Hanson, R., Wrachtrup, J. & Zhou, B. B. Quantum technologies with optically interfaced solid-state spins. *Nat. Photonics* **12**, 516–527 (2018).
6. Wang, J. et al. Multidimensional quantum entanglement with large-scale integrated optics. *Science* **360**, 285–291 (2018).
7. Qiang, X. et al. Large-scale silicon quantum photonics implementing arbitrary two-qubit processing. *Nat. Photonics* **12**, 534–539 (2018).
8. Knill, E., Laflamme, R. & Milburn, G. J. A scheme for efficient quantum computation with linear optics. *Nature* **409**, 46–52 (2001).
9. Pittman, T. B., Jacobs, B. C. & Franson, J. D. Demonstration of nondeterministic quantum logic operations using linear optical elements. *Phys. Rev. Lett.* **88**, 257902 (2002).
10. Kok, P. et al. Linear optical quantum computing with photonic qubits. *Rev. Mod. Phys.* **79**, 135–174 (2007).
11. Carolan, J. et al. Universal linear optics. *Science* **349**, 711–716 (2015).
12. Aspuru-Guzik, A. & Walther, P. Photonic quantum simulators. *Nat. Phys.* **8**, 285 (2012).
13. Gisin, N. & Thew, R. Quantum communication. *Nat. Photonics* **1**, 165 (2007).
14. Shor, P. W. & Preskill, J. Simple proof of security of the BB84 quantum key distribution protocol. *Phys. Rev. Lett.* **85**, 441–444 (2000).

15. Gisin, N., Ribordy, G., Tittel, W. & Zbinden, H. Quantum cryptography. *Rev. Mod. Phys.* **74**, 145–195 (2002).

16. Lee, H., Kok, P. & Dowling, J. P. A quantum Rosetta stone for interferometry. *J. Mod. Opt.* **49**, 2325–2338 (2002).

17. Giovannetti, V., Lloyd, S. & Maccone, L. Quantum-enhanced measurements: beating the standard quantum limit. *Science* **306**, 1330–1336 (2004).

18. Belykh, V. V. et al. Quantum interference controls the electron spin dynamics in n-GaAs. *Phys. Rev. X* **8**, 031021 (2018).

19. Dudin, Y. O., Li, L., Bariani, F. & Kuzmich, A. Observation of coherent many-body Rabi oscillations. *Nat. Phys.* **8**, 790–794 (2012).

20. Chiorescu, I., Nakamura, Y., Harmans, C. J. P. M. & Mooij, J. E. Coherent quantum dynamics of a superconducting flux qubit. *Science* **299**, 1869–1871 (2003).

21. Zibrov, A. S. et al. Experimental demonstration of laser oscillations without population inversion via quantum interference in Rb. *Phys. Rev. Lett.* **75**, 1499–1502 (1995).

22. Ward, M. B. et al. Coherent dynamics of a telecom-wavelength entangled photon source. *Nat. Commun.* **5**, 3316 (2014).

23. Boyd, R. W. *Nonlinear Optics.* 3rd edn. (Academic Press, New York, 2008).

24. Sharping, J. E. et al. Generation of correlated photons in nanoscale silicon waveguides. *Opt. Express* **14**, 12388–12393 (2006).

25. Strekalov, D. V., Marquardt, C., Matsko, A. B., Schwefel, H. G. L. & Leuchs, G. Nonlinear and quantum optics with whispering gallery resonators. *J. Opt.* **18**, 123002 (2016).

26. Kippenberg, T. J., Spillane, S. M. & Vahala, K. J. Modal coupling in traveling-wave resonators. *Opt. Lett.* **27**, 1669–1671 (2002).

27. Mandel, L. & Wolf, E. *Optical Coherence and Quantum Optics.* (Cambridge University Press, Cambridge, 1995).

28. Clemmen, S. et al. Continuous wave photon pair generation in silicon-on-insulator waveguides and ring resonators. *Opt. Express* **17**, 16558–16570 (2009).

29. Davanco, M. et al. Telecommunication-band heralded single photons from a silicon nanophotonic chip. *Appl. Phys. Lett.* **100**, 261104 (2012).

30. Azzini, S. et al. Ultra-low power generation of twin photons in a compact silicon ring resonator. *Opt. Express* **20**, 23100–23107 (2012).

31. Engin, E. et al. Photon pair generation in a silicon micro-ring resonator with reverse bias enhancement. *Opt. Express* **21**, 27826–27834 (2013).

32. Silverstone, J. W. et al. Qubit entanglement between ring-resonator photon-pair sources on a silicon chip. *Nat. Commun.* **6**, 7948 (2015).

33. Grassani, D. et al. Micrometer-scale integrated silicon source of time-energy entangled photons. *Optica* **2**, 88–94 (2015).

34. Reimer, C. et al. Generation of multiphoton entangled quantum states by means of integrated frequency combs. *Science* **351**, 1176–1180 (2016).

35. Rogers, S., Mulkey, D., Lu, X., Jiang, W. C. & Lin, Q. High visibility time-energy entangled photons from a silicon nanophotonic chip. *ACS Photonics* **3**, 1754–1761 (2016).

36. Gentry, C. M. et al. Quantum-correlated photon pairs generated in a commercial 45 nm complementary metal-oxide semiconductor microelectronic chip. *Optica* **2**, 1065–1071 (2015).

37. Mazzei, A. et al. Controlled coupling of counterpropagating whispering-gallery modes by a single Rayleigh scatter: a classical problem in a quantum optical light. *Phys. Rev. Lett.* **99**, 173603 (2007).

38. Weiss, D. S. et al. Splitting of high-Q Mie modes induced by light backscattering in silica microspheres. *Opt. Lett.* **20**, 1835–1837 (1995).

39. Guo, X., Mei, Y. & Du, S. Testing the Bell inequality on frequency-bin entangled photon pairs using time-resolved detection. *Optica* **4**, 388–392 (2017).

40. Bell, J. S. On the Einstein Podolsky Rosen paradox. *Physics* **1**, 195–200 (1964).

41. Clauser, J. F., Horne, M. A., Shimony, A. & Holt, R. A. Proposed experiment to test local hidden-variable theories. *Phys. Rev. Lett.* **23**, 800–804 (1969).

42. Thompson, R. J., Rempe, G. & Kimble, H. J. Observation of normal-mode splitting for an atom in an optical cavity. *Phys. Rev. Lett.* **68**, 1132–1135 (1992).

43. Mabuchi, H. & Doherty, A. C. Cavity quantum electrodynamics: coherence in context. *Science* **298**, 1372–1377 (2002).

44. Vahala, K. J. Optical microcavities. *Nature* **424**, 839–846 (2003).

45. Zhu, J., Özdemir, K., He, L. & Yang, L. Controlled manipulation of mode splitting in an optical microcavity by two Rayleigh scatterers. *Opt. Express* **18**, 23535–23543 (2010).

46. Lu, X., Rogers, S., Jiang, W. C. & Lin, Q. Selective engineering of cavity resonance for frequency matching in optical parametric processes. *Appl. Phys. Lett.* **105**, 151104 (2014).

47. Golter, D. A. & Wang, H. Optically driven Rabi oscillations and adiabatic passage of single electron spins in diamond. *Phys. Rev. Lett.* **112**, 116403 (2014).

48. Lu, L., Joannopoulos, J. D. & Soljačić, M. Topological photonics. *Nat. Photonics* **8**, 821–829 (2014).

49. Carmon, T., Yang, L. & Vahala, K. J. Dynamical thermal behavior and thermal self-stability of microcavities. *Opt. Express* **12**, 4742–4750 (2004).

Author contributions

Q.L. developed the original concept and theory, which were then extended by S.D.R. The device simulations and nanofabrication were performed by S.D.R. S.D.R., A.G. and U.A.J. carried out the device testing and conducted the experiment. All authors participated in the analysis of results and writing of this manuscript.

Additional information

Supplementary information accompanies this paper at https://doi.org/10.1038/s42005-019-0193-x.

Competing interests: The authors declare no competing interests.

Reprints and permission information is available online at http://npg.nature.com/reprintsandpermissions/

Publisher's note: Springer Nature remains neutral with regard to jurisdictional claims in published maps and institutional affiliations.